New insights from spectroscopy into the structure/function relationships of lipoxygenases

Edward I Solomon, Jing Zhou, Frank Neese and Elizabeth G Pavel

Spectroscopic properties of the redox-active iron in the active site of plant and mammalian lipoxygenases can now be combined with recent crystal structure determinations to obtain new insights into lipoxygenase reaction mechanisms.

Address: Department of Chemistry, Stanford University, Stanford, CA 94305, USA.

E-mail: solomon@chem.stanford.edu

Chemistry & Biology November 1997, **4**:795–808
http://biomednet.com/elecref/1074552100400795

Introduction

Lipoxygenases are non-heme iron dioxygenases that catalyze the regiospecific and stereospecific hydroperoxidation of 1,4-Z,Z-pentadiene-containing polyunsaturated carboxylic acids (Figure 1); they are believed to be present in all plants and animals (for reviews, see [1–5]). In plants, the predominant substrates of lipoxygenases are generally linoleic (18:2; eighteen carbon atoms with two double bonds) and linolenic (18:3) acids. The products of the plant lipoxygenases are further metabolized by an array of other enzymes to produce jasmonic acid and other plant hormones which are involved in plant growth and development, senescence, and responses to wounding and pathogen infection [2].

In animals, the first step in the 'linear pathway' for the metabolism of arachidonic (20:4) acid is catalyzed by lipoxygenases of different regiospecificities and stereospecificities, which lead to the generation of two classes of potent physiological effectors: leukotrienes and lipoxins [6]. Leukotrienes cause the activation, migration and adhesion of leukocytes, as well as broncho-constriction, vaso-constriction, and an increase in vascular permeability. Lipoxins may be involved in the dilation of microvasculature and the inhibition of natural killer cell cytotoxicity [7]. Other roles that lipoxygenases play in animals include the modulation of adhesion receptors in platelets, mitochondrial membrane degradation in reticulocytes [6], and tumor cell metastasis [8]. Specific inhibitors of various lipoxygenases could thus provide a breakthrough in the therapy of asthma and other inflammatory diseases which are not treatable with aspirin [9,10]. A thorough understanding of the structure of the lipoxygenases and the mechanism of the reactions they catalyze would provide the background for rational drug design.

Lipoxygenases are designated as 5-, 12-, or 15-lipoxygenases according to their ability to hydroperoxidate the indicated carbon of arachidonic acid. The three isozymes that have been isolated from mature soybean seeds are

Figure 1

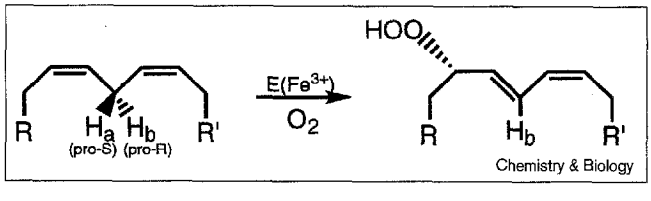

The reaction catalysed by lipoxygenases.

designated as soybean lipoxygenase-1 (SLO-1), SLO-2, and SLO-3 [11]. They have different pH profiles for activity and different regiospecificity. SLO-1, a 15-lipoxygenase, has been widely used as a model for lipoxygenase research as a result of its abundance in soybean seed, ease of purification, and stability.

This review critically examines the relationship between the structure and reactivity of the iron active site in lipoxygenases in light of the recent X-ray crystallographic and kinetic studies of SLO-1. Specifically, we will focus on the insights that spectroscopic methods have provided about the intimate details of the first coordination sphere of the iron center in lipoxygenases.

SLO-1 structure

Two X-ray crystal structures of the ferrous form of SLO-1 have been solved and coordinates are available through the Brookhaven Protein Data Bank (PDB). One structure ([12], PDB entry code 2SBL) has a resolution of 2.6 Å, and the second ([13], PDB entry code 1YGE) has a resolution of 1.4 Å; the two structures are broadly similar but have significant differences. It is important to point out the differences in the experimental conditions when comparing the two crystal structures with each other and with the results from spectroscopic studies of SLO-1. Diffraction data were collected at 100 K for 1YGE [13] and at room temperature for 2SBL [12]; crystals were grown at pH 5.6, in 0.1 M acetate buffer with 8–14% polyethylene glycol, and 28% ethylene glycol for 1YGE and at pH 7.0, in 4.5 M sodium formate, 1.0 M ammonium acetate, 600 mM LiCl, and 20 mM MES for 2SBL. In addition, the X-ray structure of SLO-3 has been solved, and the coordinates have been described in a conference abstract [14] and deposited as PDB entry 1LNH.

The two structures of SLO-1, 2SBL and 1YGE, give a consistent description of the overall SLO-1 protein structure. The enzyme is an ellipsoid of dimension 90 Å × 65 Å × 60 Å and consists of two domains. The smaller, amino-terminal domain, the function of which is unknown, comprises 146 residues and folds in a 'jelly roll' topology. The major carboxy-terminal domain consists of the remaining 693 residues and has 20 (1YGE) or 23 (2SBL) roughly parallel or antiparallel helices which form a complex helix bundle within which the iron-binding site and the potential substrate-binding site reside.

The iron-binding site

There are significant differences between the iron-binding site of SLO-1 as determined in 2SBL and 1YGE (Table 1; Figure 2). Both structures identify Nε1 of His499, His504, His690 and one C-terminal carboxylate oxygen (Ile839-O1) as ligands for the Fe^{2+} ion. A water molecule has been located trans to His690 in 1YGE; in contrast, no water molecule is found as a ligand in 2SBL. The binding of the water molecule in 1YGE is stabilized by hydrogen bonding with the unbound carboxylate oxygen of Ile839 (Ile839-O2). Oδ1 of Asn694 is 3.06 Å away from the Fe^{2+} and considered as a weak ligand for Fe^{2+} in 1YGE, whereas in 2SBL it is 3.15 Å away and not considered as a ligand. Note that the position of the iron atom in 1YGE has been reported to be associated with an uncertainty of several tenths of an angstrom, which may reflect the presence of local crystallographic disorder [13]. In 2SBL, the iron-binding site is described as a highly distorted octahedron with two adjacent unoccupied positions (4-coordinate) [12]; 1YGE has a much less distorted, octahedral Fe^{2+}-binding site (6-coordinate).

A potential substrate-binding channel

In both 1YGE and 2SBL, one large internal cavity is identified as a putative binding site for fatty acid, the enzyme's

Table 1

Coordination geometry of the Fe^{2+}-binding site in SLO-1.

Iron-ligand distances (Å)		
Ligands	1YGE	2SBL
His499Nε2	2.234	2.275
His504Nε2	2.258	2.222
His690Nε2	2.212	2.247
Asn694Oδ1	3.051	3.166
Ile839O1	2.401	2.158
Water	2.556	n.a.
Ligand-iron-ligand angle (°)*		
Angles	1YGE	2SBL
His499Nε2-Fe-His504Nε2	95.2	91.7
His499Nε2-Fe-His690Nε2	102.3	105.3
His499Nε2-Fe-Asn694Oδ2	74.9	67.9
His499Nε2-Fe-Ile839O1	167.1	158.5
His499Nε2-Fe-water	86.3	n.a.
His504Nε2-Fe-His690Nε2	105.9	100.4
His504Nε2-Fe-Asn694Oδ1	161.2	156.9
His504Nε2-Fe-Ile839O1	91.4	107.1
His504Nε2-Fe-water	97.5	n.a.
His690Nε2-Fe-Asn694Oδ1	92.0	95.5
His690Nε2-Fe-Ile839O1	86.4	82.1
His690Nε2-Fe-water	154.1	n.a.
Asn694Oδ1-Fe-Ile839O1	95.6	91.6
Asn694Oδ1-Fe-water	66.4	n.a.
Ile839O1-Fe-water	81.9	n.a.

All values were derived from PDB entries 1YGE and 2SBl. *Values obtained using software RasMac; n.a., not available.

Figure 2

The active site structure of SLO-1 from two models, **(a)** 1YGE and **(b)** 2SBL. The Fe^{2+} ion and water are shown as balls. The sidechains of His499, His504, His690 and Asn694, and carboxyl terminus of Ile839 are shown as sticks; the sidechains of Gln495 and Gln697 are shown in ball-and-stick representation. Atoms are colored by type: C, grey; O, red; N, dark blue; Fe, orange; peptide α-carbon backbone, cyan.

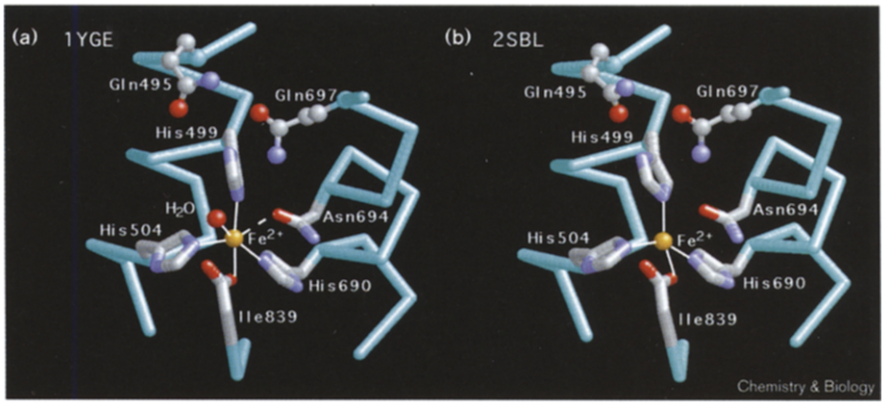

substrate, although different entrance and exit points for the fatty acid were proposed [12,13]. The substrate-binding cavity shows a bend of ~120° as it passes the water ligand of the Fe^{2+}, and the two arms of the cavity adopt a shape with approximate twofold symmetry. His499, His504, Ile839, the Fe^{2+}-ligand water molecule, and other residues directly line this cavity. The other two Fe^{2+} ligands, Asn694 and His690, have no direct contact with this cavity. The sidechain of Asn694 does, however, interact with the cavity indirectly, through a hydrogen-bonding chain which relates Asn694-Oδ1 to Gln697-Nε2 and Gln697-Oε1 to Gln495-Nε2 (Figure 2).

Gln495 and Gln697, among other residues that directly line the substrate-binding cavity, are both highly conserved among all lipoxygenases. Molecular modeling studies using both the 1YGE [15] and 2SBL [16] coordinates are consistent with this proposal. In one of the studies [16], the alkyl terminal side of the arachidonic acid substrate appears to have direct Van der Waals contact with the Gln495 sidechain, suggesting that the hydrogen-bonded chain mentioned above may play an important role in catalysis.

Conservation of active-site ligands among lipoxygenases

Alignment of the sequences of known lipoxygenases has revealed the conservation of a set of histidines which are clustered in a motif of His–$(X)_4$–<u>His</u>–$(X)_4$–<u>His</u>–$(X)_{17}$–His–$(X)_8$–His [17]. The highlighted histidines correspond to His499 and His504 in SLO-1, respectively, and have been directly identified as Fe^{2+} ligands by X-ray crystallographic studies [12,13]. Near the carboxyl terminus there is another highly conserved region which contains a His-$(X)_3$-(His/Asn) motif. The first histidine is at position 690 in SLO-1, followed by an Asn at position 694. This Asn is conserved in all plant lipoxygenases (with the exception of tomato lipoxygenase B), all mammalian 5-lipoxygenases, murine platelet 12-lipoxygenase, and human platelet 12-lipoxygenase, but it is replaced by a histidine in the rest of mammalian 12-lipoxygenases and all mammalian 15-lipoxygenases [17]. The carboxy-terminal isoleucine is conserved among all lipoxygenases except rat leukocyte 5-lipoxygenase, where it is replaced by a valine [18]. The fact that the members of the lipoxygenase family have a high level of sequence homology around the iron-binding site indicates that the SLO-1 site may serve as a good model for the iron-binding site of all lipoxygenases.

Kinetics and mechanism

The mechanism of SLO-1 has been studied in considerable detail by both steady state and rapid kinetic methods [19–30], and the reaction scheme which is consistent with the experimental data is shown in Figure 3. It was demonstrated early on that, unlike other mononuclear ferrous centers, the ferrous active site in SLO-1 does not react with dioxygen [31]. Together with other experimental results [29,32], this suggests that the first step in the catalytic cycle is the activation of the substrate by the iron in the active site [22].

The nature of the active species has been the subject of intense discussion [19–30]. Experimental evidence indicates that the ferric redox state of the iron is absolutely essential for substrate activation [27]. SLO-1 is generally purified with >90% of the active sites in the high-spin ferrous state (S = 2) [33,34]. *In vitro* oxidation to the ferric state is accomplished by reaction of ferrous SLO-1 with the hydroperoxide product [22]. Although disputed [27,28,35], it is currently believed that this conversion process is fully able to explain the lag phase observed in steady-state kinetic experiments with SLO-1 [26]. The reaction of the substrate with the minority ferric active sites produces hydroperoxide product, which in turn activates the ferrous active sites for catalysis. This highly non-linear reaction system eventually approaches a steady state where the oxygen consumption is a linear function of time, until the oxygen concentration becomes the rate-limiting factor (see [25–27] for a detailed analysis).

The intermediate formed by the reaction of the ferric enzyme with substrate (I in Figure 3) is apparently short lived (Table 2), even in the absence of dioxygen, and has therefore not yet been characterized. Both heterolytic cleavage of the C-H bond to produce a carbanion coordinated to the ferric center and homolytic cleavage to produce a substrate radical and a ferrous species have been proposed (Figure 3) [36–38].

In the absence of any direct evidence for a carbanion intermediate, most recent discussions have centered on a radical mechanism, which seems to be easier to reconcile with the available data. The radical mechanism, which is also supported by recent evidence from electron paramagnetic resonance (EPR) spectroscopy [39–41], does not require any direct interaction between dioxygen and the metal center. Pentadienyl radicals are well known to add dioxygen to form peroxyl radicals [35,42]. The resulting radical is a strong oxidant and is likely to be able to oxidize the ferrous active site to the ferric state (E*P in Figure 3) [35,43].

In the absence of dioxygen, incubation of ferric SLO-1 with fatty acid substrate leads to the ferrous enzyme and dimeric fatty acids (dimerization of two S• in Figure 3) [44]. The ferrous center in this decay product is indistinguishable from the native ferrous site by magnetic circular dichroism (MCD) spectroscopy (J.Z. and E.I.S., unpublished observations). Most recently, a novel ferric model complex has

Figure 3

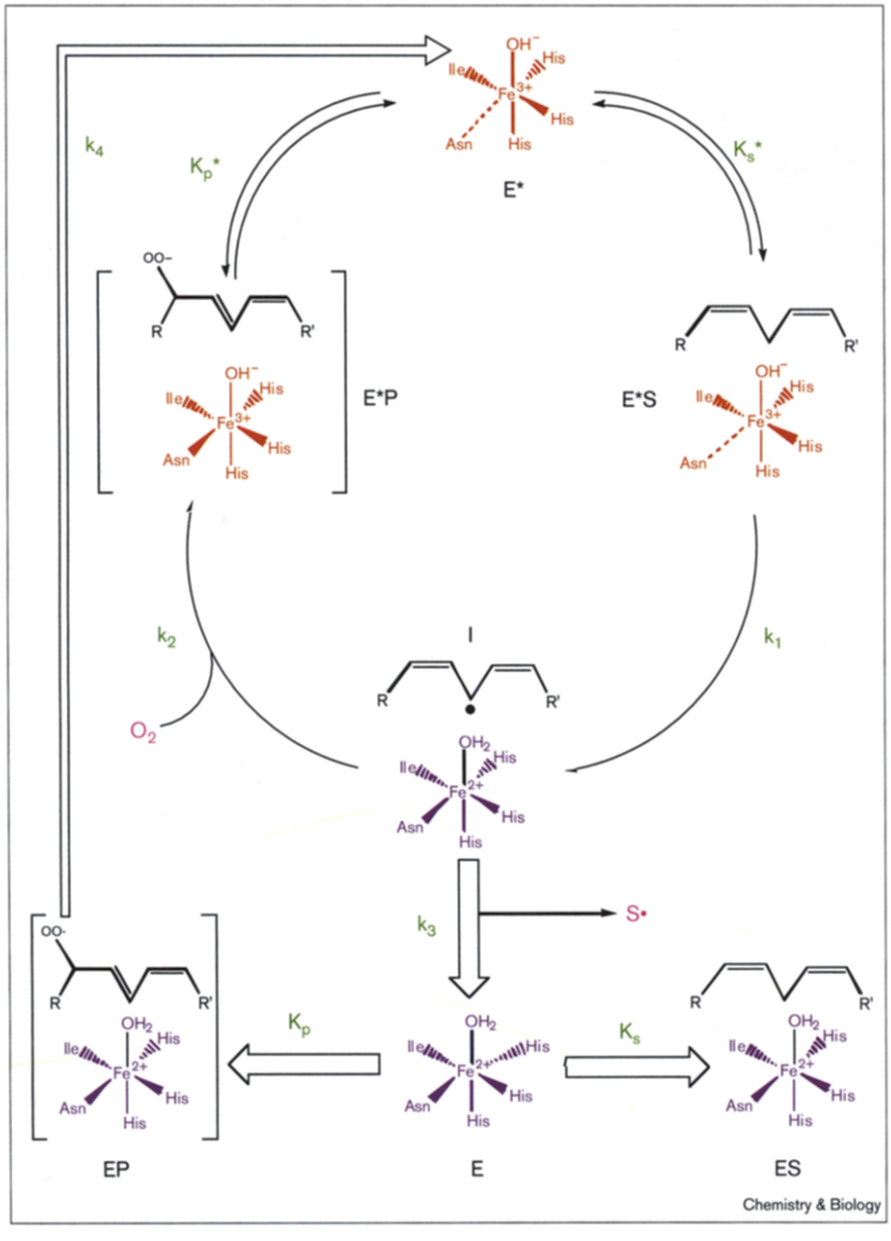

The radical mechanism for the catalytic cycle of lipoxygenases. Ferric species are shown in red and ferrous species in blue. The ferric enzyme (E*) is believed to be the active species. Binding of substrate generates the enzyme–substrate complex (E*S), which is converted, in the rate-limiting step, to the intermediate (I), shown here as a ferrous fatty acid radical complex; the structure and properties of this intermediate are, however, unknown. Reaction of dioxygen with the intermediate generates the enzyme–product complex (E*P), which has a characteristic purple color. Dissociation of product regenerates the active ferric enzyme. The intermediate can also decay into a ferrous species and a substrate radical which readily dimerizes. The ferrous enzyme is able to bind substrate to generate an 'unproductive' complex (ES) or to react with the hydroperoxide product (via the enzyme–product complex, EP) to generate the active ferric enzyme (E*). No specific structure is implied for those species enclosed in square brackets.

Table 2

Summary of published* rate and equilibrium constants for the reaction scheme in Figure 2.

k_1 (s^{-1})	k_2 ($M^{-1}s^{-1}$)	k_3 (s^{-1})	k_4 (s^{-1})	K_S (μM)	K_S^* (μM)	K_P (μM)	K_P^* (μM)
200–350	≈10^9	2,400	250	20	15–23	16	24

*Data taken from Schilstra *et al.* [27] and references therein.

been shown to be capable of carrying out similar hydrogen abstraction reactions [45]. A hybrid mechanism in which the formation of a organo-iron complex follows the hydrogen atom abstraction step has also been proposed [46,47].

It is well known that the reaction of ferric SLO-1 with the hydroperoxide product leads to a species with an absorption maximum at 580 nm ('purple' SLO-1; E*P in Figure 3) and a lifetime of several minutes at 4°C [48]. Model studies strongly suggest that this photolabile species represents a high-spin alkylperoxo complex and that the color arises from a alkylperoxo-to-iron charge transfer transition [48–51]. Importantly it has been shown by stopped-flow spectrophotometry that the purple species is formed in single-turnover experiments and must therefore be directly involved in the catalytic cycle [20,22]. Note that the mechanism shown in Figure 3 requires a reorientation of the fatty acid radical or of the product in order for the peroxyl- or alkylperoxo-oxygen to interact directly with the active-site iron as required by the presence of the charge-transfer band.

Stopped-flow kinetic investigations suggest that the rate-limiting step in the overall reaction is the substrate-activation step [20,22,29]. Measurements have shown that the rate constant k_1 in Figure 3 is associated with an unprecedented large isotope effect (≈80 [29,30,32,52]) at C-11 of linoleic acid. At the same time, the rate constant shows very little or no temperature dependence [29,30,32,52]. These observations have recently been explained by tunneling of the abstracted hydrogen atom through the potential energy barrier which separates the reactant (ferric enzyme and fatty acid substrate) from the product (ferrous enzyme and fatty acid radical) minima on the ground-state potential energy surface [52]. This purely quantum mechanical effect arises from the finite probability of a microscopic particle penetrating into a classically forbidden region where the kinetic energy of the particle is formally negative.

It has been proposed that the hydrogen atom transfer takes place in two separate steps: a proton transfer which involves tunneling and an electron transfer [52]. Given that quantum mechanics would predict the tunneling process to be reversible and the proton to be oscillating between the active site and the substrate molecule, it has been suggested [52] that the transfer of the proton is coupled to an irreversible process, namely the transfer of an electron to the ferric center. The acceptor for the proton would be a coordinated hydroxide ligand because the crystal structure of resting SLO-1 shows no other suitable base in the active site [12,13].

Spectroscopic properties of the active site of lipoxygenases

Spectroscopy of ferrous lipoxygenases

Mononuclear non-heme ferrous sites are widely present in biological systems [53], and they are usually involved in the interaction with dioxygen [54]. Although there is no evidence for direct interaction between dioxygen and the ferrous site in lipoxygenases (as discussed above) [32], the substrate-bound form of the resting ferrous enzyme most closely resembles the intermediate resulting from the substrate reaction with the Fe^{3+} lipoxygenase (I in Figure 3). Non-heme ferrous sites have been difficult to study by spectroscopic methods as they lack strong absorption features and are generally EPR silent. Magnetic susceptibility [34] and Mössbauer [55] studies have established that the iron site in resting SLO-1 is in the high-spin Fe^{2+} state with a distorted octahedral geometry. But these studies have been complicated by solvent effects (discussed in

Figure 4

Splitting patterns of the iron 3d orbitals in coordination environments of different symmetries. For high-spin (S = 2) Fe^{2+} centers, each orbital is occupied with one electron, except for the lowest one which is doubly occupied. In high-spin (S = 5/2) Fe^{3+} centers, each orbital is singly occupied. The arrows indicate typical experimental and calculated ligand field transition energies for the spin-allowed transitions of Fe^{2+} centers. There is no spin-allowed ligand field transition for Fe^{3+} centers.

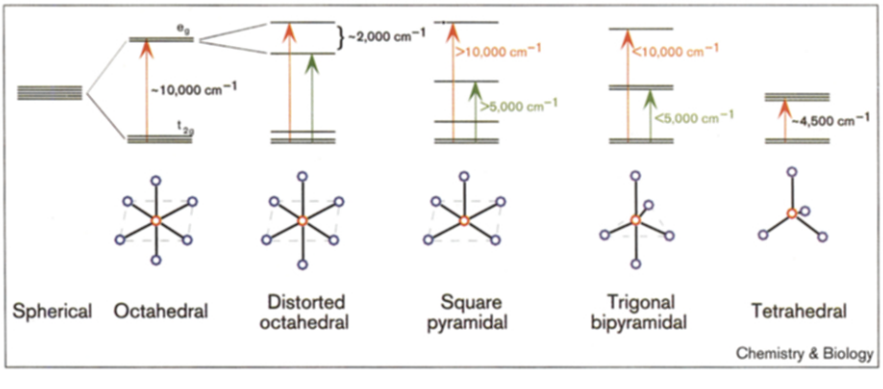

more detail below). Recently, a protocol using circular dichroism (CD) and MCD spectroscopies in the near-infrared (near-IR) spectral region in combination with ligand-field theory has been developed to explore the geometric and electronic structure of high-spin ferrous centers [53].

According to ligand field theory, the five degenerate 3d orbitals of free high-spin Fe^{2+} (electron configuration [Ar]$3d^6$) will split under different geometries imposed on the metal ion by the ligands. Figure 4 presents the Fe^{2+} 3d orbital splitting patterns for some typical symmetry environments. The octahedral six-coordinate (6C) ligand environment splits the 3d orbitals into t_{2g} and e_g sets, separated by an energy of 10Dq ≈10,000 cm^{-1} for biologically relevant N- and O-type ligands (see [53] for details). Deviation from octahedral symmetry to distorted octahedral (6C), square pyramidal (5C), and trigonal bipyramidal (5C), as well as tetrahedral (4C) geometry will further split the e_g and/or t_{2g} sets.

The energy separations have been determined experimentally using inorganic model compounds and calculated from ligand field theory [56]. In general, 6C distorted octahedral ferrous sites show two transitions around 10,000 cm^{-1} split by ~2,000 cm^{-1}; 5C square-pyramidal sites show two transitions at >10,000 cm^{-1} and >5,000 cm^{-1}; 5C trigonal bipyramidal sites show two transitions at <10,000 cm^{-1} and <5,000 cm^{-1}; and distorted 4C sites show two transitions in the 4,000–7,000 cm^{-1} region, depending on the degree of distortion. Electronic transitions between these d orbitals (d→d transitions) occur in the near-IR spectral region and are generally obscured by solvent and protein vibrations in optical absorption spectroscopy as a result of their weak extinction coefficients. However, CD and MCD spectroscopies 'filter' the weak d→d transitions of the Fe^{2+} site from the solvent and protein background and allow the direct observation of the ferrous ligand field transitions, which can be correlated with the coordination number and geometry at the ferrous center.

In addition to the excited state information mentioned above, variable-temperature, variable-field (VTVH) MCD spectroscopy provides further information about the splitting of t_{2g} orbital sets of the Fe^{2+} ion. The high-spin d^6 electron configuration of Fe^{2+} gives rise to a total spin of S = 2 with five spin components M_s = ±2, ±1, 0. The combined effects of spin-orbit coupling and a low symmetry ligand field completely lifts this fivefold spin degeneracy, even in the absence of an external magnetic field, a phenomenon called zero-field splitting. Figure 5 shows an M_s = ±2 doublet which is zero-field split by an energy δ (Figure 5b) and, for comparison, an unsplit M_s = ±2 doublet (Figure 5a), as well as the energy splitting of the levels as a result of an external magnetic field. The observed MCD intensity derives from the population difference of these sublevels at low temperature. VTVH MCD data consist of MCD intensities collected over a range of temperatures and magnetic fields at a fixed wavelength corresponding to a specific transition and are often presented in a plot of MCD intensity versus βH/2kT (where β is the Boltzmann constant and k is Planck's constant).

Figure 5c and d shows the simulated VTVH MCD data for the unsplit and zero-field-split M_s = ±2 doublets, respectively. For the unsplit doublet, all isotherms (data for a fixed temperature over a varied magnetic field) are superimposable (Figure 5c); for the zero-field-split doublet, these isotherms no longer superimpose — that is, they are nested — with the degree of nesting proportional to the magnitude of the splitting energy, δ. Fitting the

Figure 5

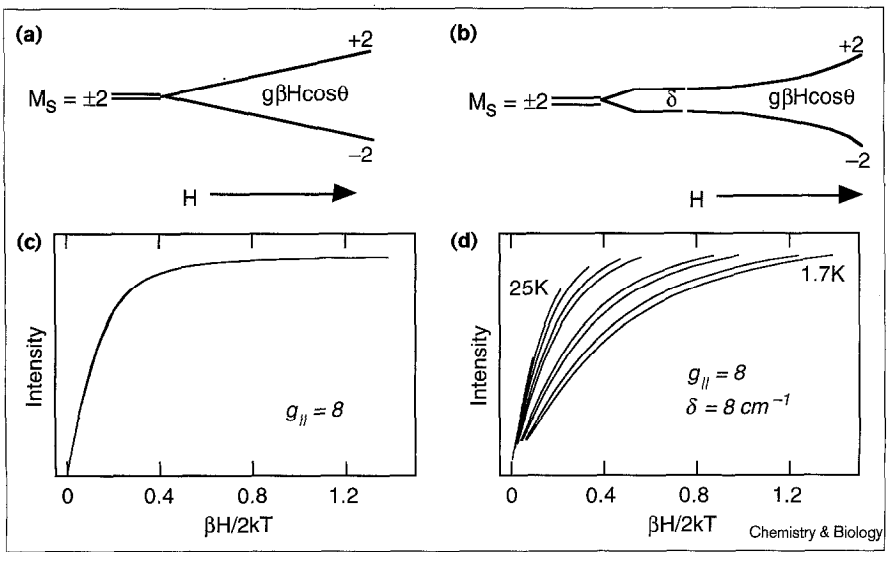

Energy splitting under external magnetic field H for **(a)** an unsplit doublet and **(b)** a zero-field-split non-Kramers doublet (in contrast to Kramers doublets, which occur for odd electron systems, even electron systems have non-Kramers doublets which are not required to be degenerate at zero magnetic field); and the VTVH MCD intensity for **(c)** an unsplit doublet and **(d)** a zero-field-split doublet.

experimental VTVH MCD data to theoretical expressions allows the estimation of δ and g (where the Zeeman splitting of a doublet is gβH), which are in turn used to construct an experimentally derived t_{2g} orbital splitting pattern [53]. Together with the excited-state analysis described above, the complete energy splittings of the iron 3d orbitals can be experimentally established.

Figure 6a shows the near-IR CD spectrum of resting SLO-1. There is a low-energy feature at <5,000 cm^{-1} and a second feature at 10,700 cm^{-1} with a shoulder at ~8,000 cm^{-1}. The low-temperature (4.2 K) near-IR MCD spectrum of resting SLO-1 is shown in Figure 6d, and has three positive peaks at <5,500, 9,200, and 10,500 cm^{-1}. Given that no ligand-field geometry of a single high-spin ferrous site can have more than two d→d transitions in the 4,000–13,000 cm^{-1} region (Figure 4), resting SLO-1 must exist in more than one form.

Anaerobic addition of substrate linoleate or the addition of methanol, ethanol, ethylene glycol, or glycerol [57] to resting SLO-1 produces a dramatic change in the near-IR CD spectrum, as shown in Figure 6b, and results in the low-temperature MCD spectrum shown in Figure 6e. Simultaneous Gaussian fitting of the CD and MCD spectra indicates a positive band at 8,600 cm^{-1} and a negative band at 10,300 cm^{-1} in the CD spectrum and two positive bands at 8,600 and 10,300 cm^{-1} in the MCD spectrum, which are consistent with a 6C ferrous site with distorted octahedral geometry. Subtraction of 60% of the 6C species signal intensity from the resting spectra and renormalization gives the CD and MCD spectra shown in Figure 6c and f, respectively. The spectra of this species, also present in resting SLO-1, have two positive d→d bands at ~5,000 and 10,600 cm^{-1}, consistent with a 5C square pyramidal geometry. So, CD and MCD studies show that resting SLO-1 exists as an approximately 40:60% mixture of 5C and 6C species [57]. The addition of monoprotic alcohols, polyprotic alcohols, or substrate linoleate to resting SLO-1 shifts the 5C-plus-6C mixture of resting SLO-1 to a purely 6C form.

Figure 6

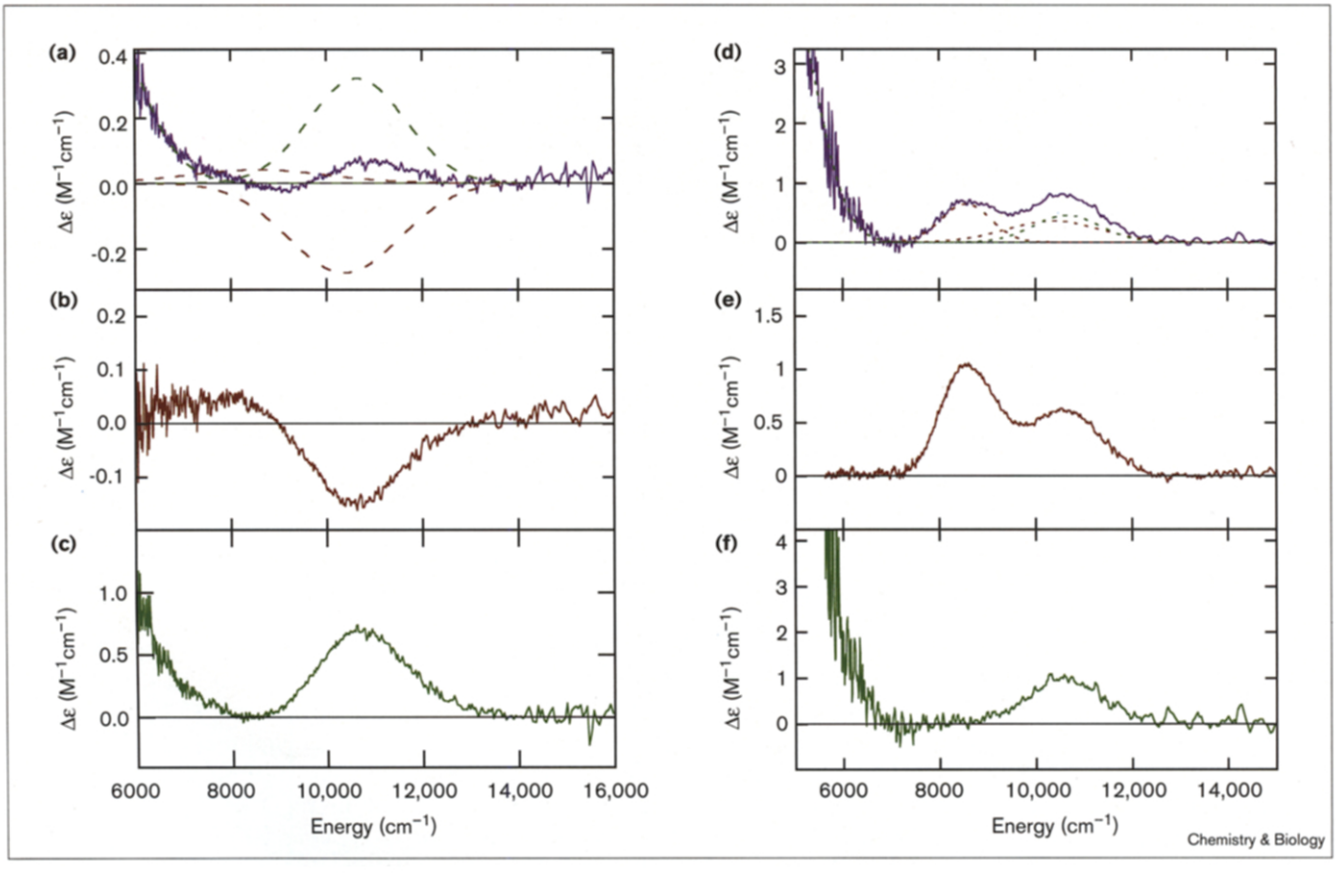

Spectra of SLO-1 (277 K CD and 5 K, 7 T MCD spectra). **(a)** CD of resting SLO-1 with Gaussian components shown in dashed lines; **(b)** CD of SLO-1 in 50% (v/v) d_3-glycerol; **(c)** data from (a) – (0.6 × data in (b)) and renormalized; **(d)** MCD of SLO-1 in saturated sucrose with Gaussian fitting components shown in dashed lines; **(e)** MCD of SLO-1 in 50% (v/v) d-glycerol; **(f)** data from (d) – (0.6 × data in (e)) and renormalized.

CD and MCD studies of human recombinant 15-lipoxygenase (15-HLO) and rabbit reticulocyte 15-lipoxygenase (15-RLO) provide further information about the protein ligand responsible for this coordination flexibility at the Fe^{2+} active site [57]. In contrast to the situation for SLO-1, glycerol does not perturb the near-IR CD spectra of resting 15-HLO or 15-RLO. Their low temperature MCD spectra are shown in Figure 7. For 15-HLO, a band at 8750 cm^{-1} with a shoulder at ~10,700 cm^{-1} indicates a 6C ferrous site. The similar MCD spectrum of 15-RLO (band at 8650 cm^{-1} and shoulder at ~10,300 cm^{-1}) is also consistent with a 6C ferrous site in the enzyme. Therefore, substitution of asparagine with histidine leads to a pure 6C Fe^{2+} site in these mammalian lipoxygenases.

Figure 7

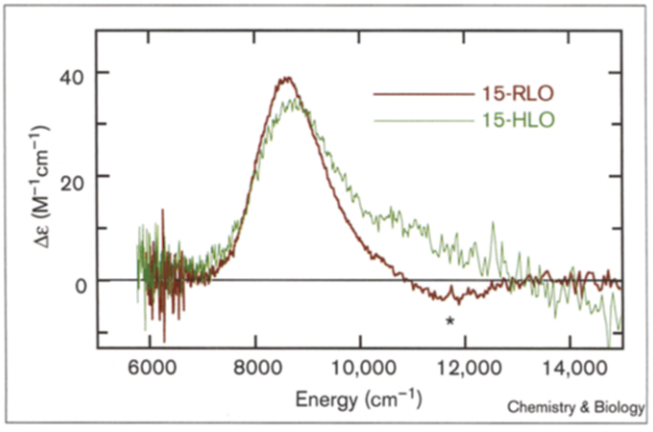

Low temperature (5 K) near-IR MCD of 15-RLO and 15-HLO at 7 T magnetic field strength (* indicates a heme impurity).

VTVH MCD studies of resting SLO-1 (6C species), 15-HLO, and 15-RLO indicate very different ground-state resting 15-RLO (right). The SLO-1 data show a much larger degree of nesting than observed for 15-RLO. Analyses of these data give $\delta = 13$ cm^{-1}, $g = 8$ for the 6C species of SLO-1 and $\delta \approx 4$ cm^{-1}, $g \approx 9$ for 15-RLO. The δ values are consistent with the t_{2g} orbital splittings shown at the bottom of Figure 8, and the difference can be attributed to a stronger histidine ligand replacing the asparagine ligand in the axial direction (z) of the Fe^{2+} site [57].

Another physical technique which has been successfully applied to both the ferrous and ferric active sites in lipoxygenases [47,57,58] is X-ray absorption spectroscopy (XAS) and the associated fine structure analysis (EXAFS) [59]. While EXAFS is most sensitive to metal-ligand bond distances, the pre-edge region of the XAS spectrum contains important information about spin state and coordination geometry [59]. The pre-edge intensity observed in XAS spectra at the iron K-edge (at the K-edge, an electron is excited from a 1s orbital into the valence orbitals of the metal atom) is ascribed to a 1s→3d electric dipole forbidden transition which gains intensity through 3d/4p mixing, while the EXAFS spectrum reflects scattering of ejected electrons by the ligands around the iron [59].

Empirically, the pre-edge features of SLO-1 in glycerol look much more similar in shape and intensity to those of 6C ferrous model complexes and are quite different from those of 4C and 5C models, indicating that resting SLO-1 in glycerol has a 6C ferrous site [57]. EXAFS studies of resting SLO-1 in glycerol show that the Fe^{2+} site has 5 ± 1 O/N ligands at ~2.16 Å, an average bond length consistent with those of 6C models [57]. Early EXAFS studies [58] on resting SLO-1 indicated 6 ± 1 N/O ligands at 2.05–2.09 Å with a maximum variance of 0.09 Å, including 4 ± 1 imidazole ligands. These studies may be complicated by the fact that under the experimental conditions of the study, resting SLO-1 exists as mixture of 5C and 6C species [57]. Another XAS study [46] reported a change in the ferrous coordination environment upon addition of methanol or glycerol. Although the XAS and EXAFS studies on resting SLO-1 are also complicated by its mixture characteristics, the addition of 0.1% methanol or 20% glycerol to resting SLO-1 result in a pure 6C species. Taken together, these XAS and EXAFS studies are consistent with the CD and MCD results. Iron K-edge XAS and EXAFS studies of resting 15-HLO and 15-RLO in glycerol have also confirmed the results from CD and MCD studies [57].

Correlating the spectroscopic studies with the two crystal structures of SLO-1, the potential ligand that would show coordination flexibility is Asn694-Oδ1, which is 3.17 Å away in the 2SBL structure of SLO-1 [12] and 3.05 Å away in the 1YGE structure [13] from the Fe^{2+}. Spectroscopically, both of these distances place Asn694-Oδ1 too far from the ferrous ion to be a reasonable ligand; as discussed above, there is significant disorder in the distance between the sidechain amide oxygen of Asn694 and the Fe^{2+} ion in the crystal. This is consistent with the CD and MCD studies of resting SLO-1, which show that the enzyme exists as a mixture of 5C and 6C species. The substitution of the weak asparagine ligand by a stronger histidine ligand, as in mammalian 15-lipoxygenases, would result in a pure 6C environment with histidine bound tightly to the Fe^{2+} ion; and this has indeed been experimentally observed in the CD, MCD and X-ray absorption studies of 15-HLO and 15-RLO [57]. Finally, the sidechain of Asn694 in SLO-1 is related to the substrate-binding cavity through a hydrogen-bonding network [13] (as discussed above). The binding of substrate or alcohols in this cavity might interrupt the hydrogen-bonding network and could result in a stronger

Figure 8

(a) VTVH MCD of SLO-1 (6C species; left) and 15-RLO (right). Experimental data are shown as blue markers; fits to the data are shown as red lines. **(b)** Comparison of SLO-1 (6C) and 15-RLO t_{2g} orbital splittings (LF, ligand field).

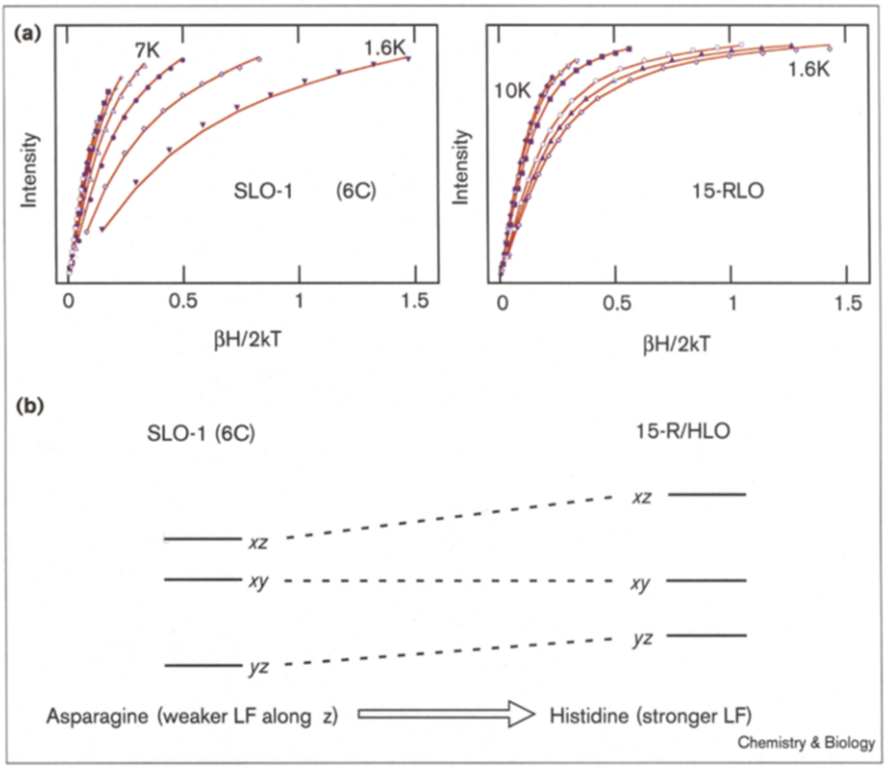

interaction between the Asn694 amide oxygen and the Fe^{2+} ion, thus shifting the 5C-plus-6C mixture to a pure 6C species.

Spectroscopy of ferric lipoxygenases

In the case of the ferrous active site, direct observation of the weak ligand field transitions has been instrumental in experimentally establishing the presence of coordination flexibility at the active site in SLO-1. Unfortunately a similar approach is not feasible for the ferric active site, which has been shown to exist in the high-spin (S = 5/2) state [33]. In monomeric high-spin ferric centers, each of the five 3d orbitals of the iron (see Figure 4) is occupied with one electron to produce a sixfold spin-degenerate ground state ($^6A_1$ state). As all five unpaired electrons have the same spin, an electron can only be excited within this subset if the excitation is accompanied by a change of spin of the electron (a 'spin flip') which produces a four-fold spin-degenerate excited state. This is a quantum mechanically forbidden process, and therefore monomeric S = 5/2 ferric centers show extremely weak absorption bands ($\varepsilon < 1\ M^{-1}\ cm^{-1}$). These bands have been observed in SLO-1 [48], but their information content in terms of the active-site structure is not as high as in the case of ferrous centers. In contrast to many ferrous sites, ferric centers show ligand-to-metal charge-transfer transitions: for example, in SLO-1 there are imidazole→Fe(III) ligand-to-metal charge-transfer transitions in the 350 nm region. These can be probed by VTVH MCD spectroscopy and geometric information can be extracted [48].

Given the difficulty in probing ferric centers by excited state spectroscopic methods, EPR spectroscopy and related methods are usually employed [60]. The EPR signals of the ferric active site in SLO-1 have been studied and used in a variety of ways to obtain biochemically relevant information [31,61–64]. Studies with ^{17}O labeled water have demonstrated that a water-derived ligand coordinates to the Fe^{3+} active site [63]. The spectral correlations described below have important mechanistic consequences and require some background information about EPR spectroscopy and the physical origin of the observed spectral features.

EPR spectroscopy allows the detection of magnetic dipole transitions in the microwave region of the electromagnetic spectrum [60]. From the position of a resonance line, one can extract characteristic g values using the relation $g = 0.7147\nu/H_{res}$, where ν is the operating frequency of the spectrometer (in GHz) and H_{res} the resonance position (in Gauss). In principle, a ferric center can give rise to three resonance lines in an EPR spectrum, where each line is related to a different orientation of the magnetic field with respect to a molecular axis system [60]. Idealized EPR spectra for typical ferric centers are shown in Figure 9a and are phenomenologically classified by their degree of 'rhombicity'.

A ferric center which displays an intense derivative shaped signal in the region around g = 6 and a weak resonance around g = 2 is said to be 'axial' (Figure 9a, graph i). The resonance around g = 6 can split into two components, as shown in Figure 9a (graph ii). The signal is then said to be of 'intermediate rhombicity'. In the limit of 'complete rhombicity', a single intense signal in the region around g = 4.28 is observed (Figure 9a, graph iii). Axial EPR patterns are frequently observed for high-spin ferric heme proteins, but are very uncommon for non-heme ferric centers. As shown in Figure 10, the spectrum displayed by SLO-1 (Figure 10a) is almost completely axial [48,49,61,62], while that of 15-RLO (Figure 10b) is completely rhombic. This unusual spectral behavior can be directly correlated to the reactivity of the active site.

The classification of spectra into axial or rhombic forms can be put on a more quantitative basis when the two parameters D and E/D are introduced. They describe the zero-field splitting of the S = 5/2 electronic ground state into three pairs of levels (Kramers doublets) with $M_S = \pm 1/2$, $\pm 3/2$ and $\pm 5/2$ [60,65], (Figure 9b). When a magnetic field is turned on, the degeneracy of each of the doublets is lifted and transitions between the magnetic-field-split components can be observed (Figure 9b). Whereas D describes the overall strength of the zero-field splitting, E/D is directly related to the rhombicity. By definition, E/D can vary only between 0 (axial) and 1/3 (completely rhombic). If D is much larger than the energy quantum of the EPR spectrometer, hν, a simple method is available to extract the value of E/D from the experimental spectrum [65]. Figure 9c shows the relation between the resonance position (measured by its corresponding g value) and the rhombicity. The three panels correspond to the three possible resonance lines that can be observed for each of three transitions depicted in Figure 9b. The E/D value is found by drawing horizontal lines from the experimentally determined resonance positions and determining the abcissa-value at the intersection point of

Figure 9

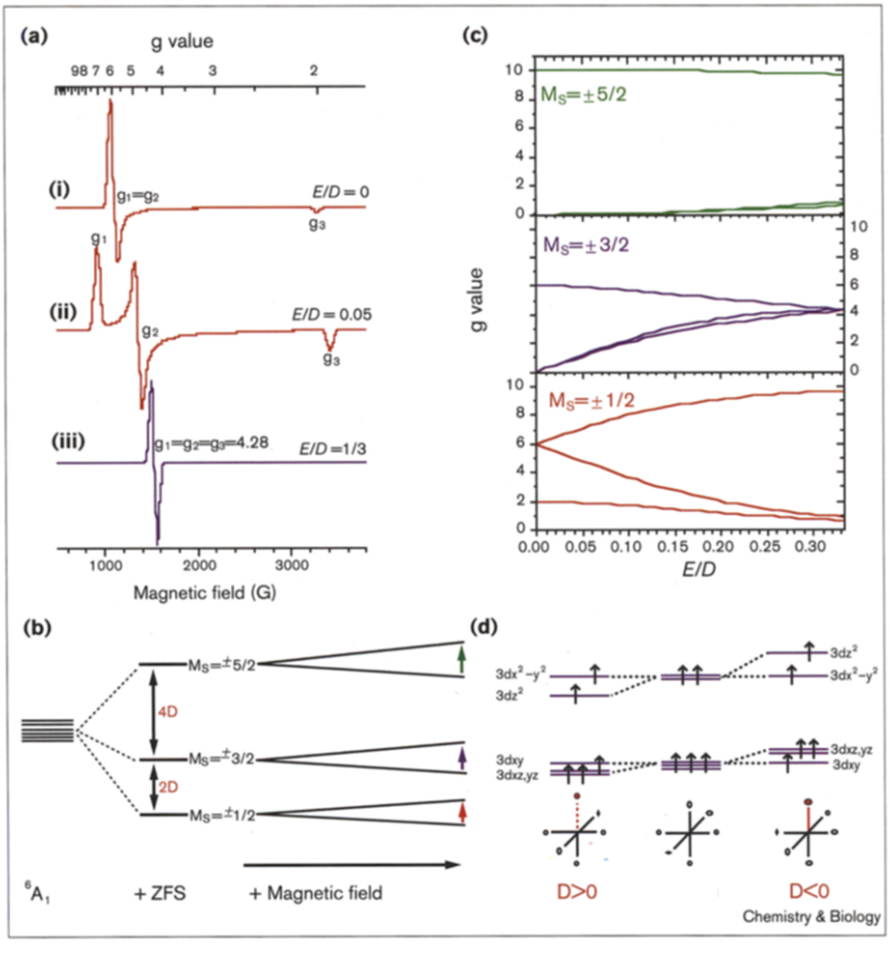

(a) Idealized EPR spectra for a monomeric high-spin ferric center showing the progression from (i) the purely axial case ($E/D = 0$) to (iii) the purely rhombic limit ($E/D = 1/3$). The positions of the characteristic g values g_1, g_2 and g_3 are indicated. Note that these are also called g_x, g_y, g_z or g_{max}, g_{mid}, and g_{min} in the literature. **(b)** Schematic illustrating the ground-state splitting in ferric centers. The sixfold spin-degenerate electronic ground state of a ferric center undergoes a zero field splitting into three Kramers doublets (labeled $M_S = \pm 1/2$, $\pm 3/2$ and $\pm 5/2$, respectively) in the absence of a magnetic field. In the axial case, the splittings are given by 2 | D | and 4 | D | respectively. In the rhombic case, the splittings are 3.528 | D |. Note that for $D < 0$ the level scheme is the reverse of that shown here. Application of a magnetic field further removes the degeneracy and allows the detection of magnetic dipole transitions between the magnetic-field-split sublevels by EPR spectroscopy. **(c)** Resonance positions observed in an EPR spectrum of a ferric center for each of the transitions depicted in (b) as a function of the rhombicity parameter E/D. The resonance position is related to the effective g value by H_{res} (in Gauss) = 0.7147 ν (in GHz) / g_{eff}. Up to three peaks are observed for each transition shown in (b), corresponding to the three principal orientations of the molecule relative to the external magnetic field direction. **(d)** Relationship between the electronic and geometric structure of a ferric center and the sign of the D value. For octahedral coordination the five iron 3d orbitals split into a π-antibonding t_{2g} set ($3d_{xy}$, $3d_{xz}$, $3d_{yz}$) and a σ-antibonding e_g set ($3d_z2$, $3d_x2_{-y}2$) (see Figure 4). A weak ligand field along the +z axis (left) leads to a decrease in the energy of the $3d_z2$ orbital and a positive D value; a strong ligand field along the +z axis leads to an increase in the energy of the $3d_z2$ orbital and a negative D value (right).

Figure 10

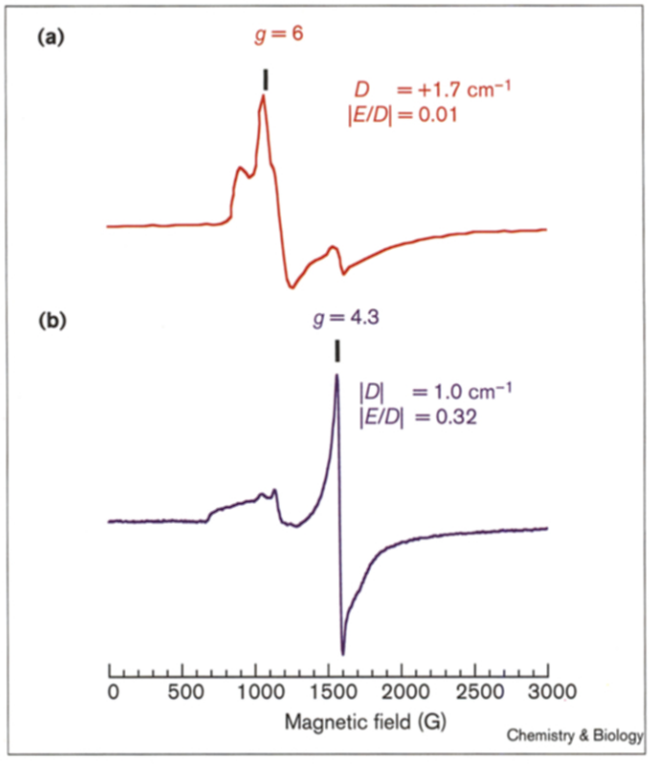

Low temperature (10 K) continuous wave X-band (9.5 GHz) EPR spectra observed for ferric lipoxygenases. **(a)** EPR spectrum of ferric SLO-1, showing almost pure axial symmetry. **(b)** EPR spectrum of ferric 15-RLO, showing almost pure rhombic symmetry.

the these lines with the theoretical curves. The value of D is more difficult to determine and will in most cases require spectra recorded at several different temperatures. It is important that D can be either positive or negative: a positive sign indicates that the $M_S = \pm 1/2$ doublet is lowest in energy, while a negative sign leads to the $M_S = \pm 5/2$ doublet being lowest.

Both D and E/D contain vital information about the electronic structure of a ferric center [48,49,66,67]. The t_{2g} orbitals ($3d_{xy}$, $3d_{xz}$ and $3d_{yz}$) are π-antibonding with the ligands while the e_g orbitals ($3d_{x^2-y^2}$ and $3d_{z^2}$) are σ-antibonding (Figure 4). Removal of a ligand from the +z direction leads to a lowering of the energy of the $3d_{z^2}$ orbital and to lesser extent of the $3d_{xz}$ and $3d_{yz}$ orbitals. An increase in the ligand field strength along this direction leads to an opposite splitting pattern (Figure 9d). Theoretical analysis [48,49,66,67] shows that the splitting between the e_g orbitals dominates the effects of the ligand environment on the D and E/D values, that the sign of D is positive if the $3d_{z^2}$ orbital is energetically below the $3d_{x^2-y^2}$ orbital and negative for the reverse situation, and that small E/D values (axial EPR patterns) can only be obtained if the ligand field strength seen by the ferric ion has a unique weak or a unique strong component along one direction.

Application of these correlations to the ferric active sites of lipoxygenases has led to important insights into the geometric and electronic structure of the active site [48,49]. EPR spectra of ferric SLO-1 invariably show the presence of several species [48,61,62,68] which can be quantified by advanced simulation techniques [61]. In the presence of alcohols, a pure axial form is observed ($|E/D| \approx 0.02$), while removal of the reaction product by high performance liquid chromatography (HPLC) leads to a rhombically perturbed but close-to-axial species with $|E/D| \approx 0.07$ [62].

The important point is that the E/D values observed for both forms of SLO-1 are close to the axial limit (Figure 10a), so a unique weak or strong direction must exist in the ligand fields of all species in ferric SLO-1. The D value was determined to be positive for the pure axial species [48,49], and so the unique component must be a weak direction. This means that one of the Fe^{3+} ligands in SLO-1 is involved in a very weak donor bond.

Insights into the nature of the weak ligand have been obtained by studying the EPR spectra of 15-lipoxygenases from humans and rabbits [49,56]. The iron ligands of 15-HLO and 15-RLO are identical and the spectroscopic behavior of the active sites is very similar. The coordination sphere of the iron in both mammalian enzymes is similar to that of SLO-1 except for the substitution of Asn694 by a histidine residue. This change in ligation is accompanied by a dramatic change in the EPR spectral behavior of 15-HLO and 15-RLO. Both mammalian enzymes show rhombic EPR patterns (Figure 10b), signifying a relatively equal ligand field strength produced by each ligand and consistent with the expectation that histidine is a stronger ligand for Fe^{3+} than is asparagine. Thus, as in the case of the Fe^{2+} active site, the weak ligand present in Fe^{3+} SLO-1 can plausibly be assigned to Asn694 [49,56]. In summary, EPR spectroscopy establishes the ferric active site in SLO-1 as being pseudo-5C, with the weak ligand being assigned as Asn694.

The available EXAFS information for the ferric site in SLO-1 is consistent with 6 ± 1 ligands at distances 2.11 Å (3N,2O)/1.88 Å (1O) [46] or 1.90 Å (3O)/2.11 Å (3N) [58]. A thorough XAS/EXAFS study concluded that, on the basis of pre-edge intensities and bond-valence sum analysis, the spectra of Fe^{3+} SLO-1 are most easily matched with a 6C ferric active site [46]. It is important to point out that this conclusion is not inconsistent with the results from EPR spectroscopy. Whereas XAS/EXAFS is primarily sensitive to the geometric structure of the site, EPR is sensitive to its electronic structure. The EPR data require the presence of a weak iron–asparagine bond. A weak ligand field would certainly be created by a ligand at a large distance (>2.5 Å), but it is also consistent with a closer ligand whose orbitals do not strongly interact with the iron 3d orbitals, as appears

to be the case for an asparagine oxygen. For 15-RLO and 15-HLO, it is likely that the ferric ion in both enzymes is 6C with four histidine ligands, the terminal carboxylate oxygen, and an OH^- ion.

Mechanistic insights from spectroscopic studies

The key step of the lipoxygenase mechanism outlined in Figure 3 is the abstraction of a hydrogen atom by the active site ferric ion, as shown in Figure 11. The spectroscopic studies on Fe^{3+} and Fe^{2+} lipoxygenases discussed above have yielded significant insights into how this step might be achieved by SLO-1. The axial EPR signals of the substrate-analog-bound form of Fe^{3+} SLO-1 demonstrate that the Fe^{3+} site (Figure 11a) has a pseudo-5C geometry with a very weak iron-asparagine bond. Alternatively, CD, MCD and X-ray absorption studies of the substrate-bound form the Fe^{2+} SLO-1 show that the Fe^{2+} site (Figure 11b) is a pure 6C site which has six ligands with comparable ligand field strengths.

Assuming that the mechanism shown in Figure 3 is correct, the ability of lipoxygenases to carry out effective hydrogen abstraction reactions requires the coordinated water to have a strong OH bond in the Fe^{2+} state. Given that hydrogen abstraction involves protonation of the OH^- ligand and reduction of the iron, the driving force of the overall reaction in Figure 11 can be related to the pK_a of the coordinated water and to the redox potential of the site [69] (The Gibbs free energy of the reaction shown in Figure 11 can be related to the reduction potential ($E^{o\prime}$) of the Fe^{3+}/Fe^{2+} couple and the pK_a of Fe^{2+}-OH_2 in the following equation: $\Delta G^{o\prime} = -(FE^{o\prime} + 2.303 \bullet RTpK_a) + DE + C$, in which F is Faraday's constant, DE is the free energy of the C-H bond cleavage reaction, and C is a constant.) A high redox potential is required to provide a sufficient driving force for electron transfer, while a high pK_a of the Fe^{2+}-coordinated water is required for proton transfer. Apparently both requirements are realized in the active site of SLO-1 and are directly reflected in its spectroscopic properties. The high potential of the Fe^{3+}/Fe^{2+} couple in SLO-1 is documented by the fact that Fe^{3+} SLO-1 is converted to Fe^{2+} SLO-1 even in the absence of reducing agents [70], and a lower limit of $E^{0\prime} = +600 \pm 100$ mV has been estimated [71]. This is readily explained by the finding that the ferric active site in SLO-1 is best described as pseudo-5C, as discussed above. Compared to a 6C site, the electron density at the ferric center is reduced in a pseudo-5C center, leading to a destabilization of the Fe^{3+} state and hence an increase in the redox potential of the metal ion. Alternatively, a 6C ferrous site ensures a high pK_a of the coordinated water by decreasing the inductive polarization of the OH bond.

The mechanism outlined above attributes an important role to the Asn694 ligand in the catalytic mechanism of SLO-1. Consequently, exchange of this ligand for a stronger coordinating ligand, such as histidine, is expected to lower the catalytic efficiency of lipoxygenases. As noted above, sequence comparisons have revealed that all ligands with the exception of Asn694 are highly conserved. Alternatively, the position of Asn694 can be occupied by a histidine residue. A survey of the published values for k_{cat} and K_M suggests that the K_M values for all lipoxygenases are similar. By contrast the k_{cat} values for the hydroperoxidation reaction of the enzymes in which histidine replaces Asn694 were found to be smaller than that of SLO-1; for example, the K_M and k_{cat} values for SLO-1 are 12 μM and 280 s^{-1}, respectively [11,22], whereas the corresponding values for 15-RLO are ~12 μM and ~30 s^{-1} [72]. Of course, it can not be expected that a simple mutation from histidine to asparagine in any of the enzymes in which histidine replaces Asn694 will automatically yield highly active lipoxygenases: efficient catalytic activity depends on a complicated interplay of many factors. Nevertheless, the information available at present is consistent with an important role for the coordinatively flexible Asn694 ligand in the catalytic cycle of lipoxygenases.

Figure 11

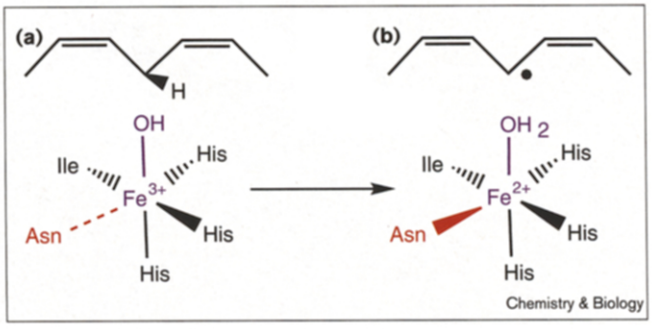

Geometric and electronic structure contributions to the rate-determining hydrogen-atom abstraction step in the catalytic cycle of lipoxygenases.

Acknowledgements

Our research is supported by the National Institutes of Health (GM40392). F.N. thanks the Deutsche Forschungsgemeinschaft for a postdoctoral fellowship.

References

1. Gardner, H.W. (1991). Recent investigations into the lipoxygenase pathway of plants. *Biochim. Biophys. Acta* **1084**, 221-239.
2. Siedow, J.N. (1991). Plant lipoxygenase: structure and function. *Annu. Rev. Plant Physiol. Plant Mol. Biol* **42**, 145-188.
3. Ford-Hutchinson, A.W., Gresser, M. & Young, R.N. (1994). 5-lipoxygenase. *Annu. Rev. Biochem* **63**, 383-417.
4. Schewe, T., Rapoport, S.M. & Kuehn, H. (1986). Enzymology and physiology of reticulocyte lipoxygenase: comparison with other lipoxygenases. *Adv. Enzymol. Relat. Areas Mol. Biol* **58**, 191-272.
5. Yamamoto, S. (1992). Mammalian lipoxygenases: molecular structures and functions. *Biochim. Biophys. Acta* **1128**, 117-131.
6. Sigal, E. (1991). The molecular biology of mammalian arachidonic acid metabolism. *Am. J. Physiol.* **260**, L13-L28.

7. Samuelsson, B., Dahlen, S.-E., Lindgren, J.A., Rouzer, C.A. & Serhan, C.N. (1987). Leukotrienes and lipoxins: structures, biosynthesis, and biological effects. *Science* **237**, 1171-1176.
8. Honn, K.V., *et al.*, & Hagmann, W. (1994). 12-Lipoxygenases and 12(S)-HETE: role in cancer metastasis. *Cancer Metastasis Rev.* **13**, 365-396.
9. Sorkness, C.A. (1997). The use of 5- lipoxygenase inhibitors and leukotriene receptor antagonists in the treatment of chronic asthma. *Pharmacotherapy* **17**, 50S-54S.
10. Musser, J.H. & Kreft, A.F. (1992). 5-lipoxygenase: properties, pharmacology, and the quinolinyl(bridged)aryl class of inhibitors. *J. Med. Chem.* **35**, 2501-2524.
11. Axelrod, B., Cheesbrough, T.M. & Laakso, S. (1981). Lipoxygenase from soybeans. *Methods Enzymol.* **71**, 441-451.
12. Boyington, J.C., Gaffney, B.J. & Amzel, L.M. (1993). The three-dimensional structure of an arachidonic acid 15-lipoxygenase. *Science* **260**, 1482-1486.
13. Minor, W., *et al.*, & Axelrod, B. (1996). Crystal structure of soybean lipoxygenase L-1 at 1.4 Å resolution. *Biochemistry* **35**, 10687-10701.
14. Funk, M.O.J., Skrzypczak-Jankun, E. & Amzel, L.M. (1996). The three-dimensional structure of soybean lipoxygenase L3 and a comparison with the L1 isoenzyme. *FASEB J.* **10**, A1109.
15. Gan, Q.-F., Browner, M.F., Sloane, D.L. & Sigal, E. (1996). Defining the arachidonic acid binding site of human 15-lipoxygenase. *J. Biol. Chem.* **271**, 25412-25418.
16. Prigge, S.T., Boyington, J.C., Gaffney, B.J. & Amzel, L.M. (1996). Lipoxygenases: structure and function. In *Lipoxygenase and Lipoxygenase Pathway Enzymes* (Piazza, G., ed.), pp 1-32, AOCS Press, Champaign, Illinois.
17. Sloane, D.L. (1996). Exploring the structure and function of mammalian lipoxygenases by site-directed mutagenesis. In *Lipoxygenase Lipoxygenase Pathway Enzymes* (Piazza, G., ed.), pp 57-79, AOCS Press, Champaign, Ill.
18. Sigal, E., *et al.*, & Jadel, J.A. (1988). Molecular cloning and primary structure of human 15-lipoxygenase. *Biochem. Biophys. Res. Commun.* **157**, 457-464.
19. Lagock, J.W., Emken, E.A., Law, J.H. & Kezdy, F.J. (1976). Kinetic analysis of soybean lipoxygenase on linoleic acid. *J. Biol. Chem.* **251**, 6001-6006.
20. Egmond, M.E., Fasella, P.M., Veldink, G.A., Vliegenthart, J.F.G. & Boldingh, J. (1977). On the mechanism of action of soybean lipoxygenase-1. *Eur. J. Biochem.* **76**, 469-479.
21. Hamberg, M. & Samuelsson, B. (1967). On the specificity of the oxygenation of unsaturated fatty acids catalyzed by soybean lipoxidase. *J. Biol. Chem.* **242**, 5329-5335.
22. Veldink, G.A. & Vliegenthart, J.F.G. (1984). Lipoxygenases, nonheme iron-containing enzymes. *Adv. Inorg. Biochem.* **6**, 139-161.
23. DeGroot, J.J.M., Carssen, G.J., Vliegenthart, J.F.G. & Boldingh, J. (1973). Detection of linoleic acid radicals in the anaerobic reaction of lipoxygenase. *Biochem. Biophys. Acta* **326**, 279-284.
24. Aoshima, H., Kajiwara, T., Hatanaka, A., Nakatani, H. & K, H. (1975). Biosynthesis of leaf alcohol. Kinetic study of lipoxygenase activation process caused by hydroperoxylinoleic acid. *Agric. Biol. Chem.* **39**, 2255-2257.
25. Schilstra, M.J., Veldink, G.A., Verhagen, J. & Vliegenthart, J.F.G. (1992). Effect of hydroperoxide on lipoxygenase kinetics. *Biochemistry* **31**, 7692-7699.
26. Schilstra, M.J., Veldink, G.A. & Vliegenthart, J.F.G. (1993). Kinetic analysis of the induction period in lipoxygenase catalysis. *Biochemistry* **32**, 7686-7691.
27. Schilstra, M.J., Veldink, G.A. & Vliegenthart, J.F.G. (1994). The dioxygenation rate in lipoxygenase catalysis is determined by the amount of iron(III) lipoxygenase in solution. *Biochemistry* **33**, 3974-3979.
28. Wang, Z.X., Killilea, S.D. & Srivastava, D.K. (1993). Kinetic evaluation of substrate-dependent origin of the lag phase in soybean lipoxygenase-1 catalyzed reactions. *Biochemistry* **32**, 1500-1509.
29. Glickman, M.H. & Klinman, J.P. (1995). Nature of rate-limiting steps in the soybean lipoxygenase-1 reaction. *Biochemistry* **34**, 14077-14092.
30. Jonsson, T., Glickman, M.H., Sun, S.J. & Klinman, J.P. (1996). Experimental evidence for extensive tunneling of hydrogen in the lipoxygenase reaction: implications for enzyme catalysis. *J. Am. Chem. Soc.* **118**, 10319-10320.
31. Feiters, M.C., *et al.*, & Vliegenthart, J.F.G. (1985). Substrate fatty acid activation in soybean lipoxygenase-1 catalysis. *Biochem. Biophys. Acta* **831**, 302-305.
32. Glickman, M.H. & Klinman, J.P. (1996). Lipoxygenase reaction mechanism: demonstration that hydrogen abstraction from substrate precedes dioxygen binding during catalytic turnover. *Biochemistry* **35**, 12882-12892.
33. Cheesbrough, T.M. & Axelrod, B. (1983). Determination of the spin state or iron in native and activated soybean lipoxygenase 1 by paramagnetic susceptibility. *Biochemistry* **22**, 3837-3840.
34. Petersson, L., Slappendel, S. & Vliegenthart, J.F.G. (1985). The magnetic susceptibility of native soybean lipoxygenase-1. Implications for the symmetry of the iron environment and the possible coordination of dioxygen to Fe(II). *Biochem. Biophys. Acta* **828**, 81-85.
35. Nelson, M.J. & Seitz, S.P. (1994). The structure and function of lipoxygenase. *Curr. Opin. Struct. Biol.* **4**, 878-884.
36. DeGroot, J.J.M.C., *et al.*, & Van Gelder, B.F. (1975). Demonstration by EPR spectroscopy of the functional role or iron in soybean 1-lipoxygenase. *Biochem. Biophys. Acta.* **377**, 71-79.
37. Corey, E.J. & Nagata, R. (1987). Evidence in favour of an organoiron-mediated pathway for lipoxygenation of fatty acids by soybean lipoxygenase. *J. Am. Chem. Soc.* **109**, 8107-8108.
38. Corey, E.J. & Walker, C. (1987). Organoiron-mediated oxygenation of allylic organotin compounds. A possible chemical model for enzymatic lipoxygenation. *J. Am. Chem. Soc.* **109**, 8108-8109.
39. Chamultriat, W. & Mason, R.P. (1989). Lipid peroxyl radical intermediates in the peroxidation of polyunsaturated fatty acids by lipoxygenase. *J. Biol. Chem.* **264**, 20968-20973.
40. Nelson, M.J. & Cowling, R.A. (1990). Observation of a peroxyl radical in samples of 'purple' lipoxygenase. *J. Am. Chem. Soc.* **112**, 2820-2821.
41. Nelson, M.J., Cowling, R.A. & Seitz, S.P. (1990). Enzyme-bound pentadienyl and peroxyl radicals in purple lipoxygenase. *Biochemistry* **29**, 6897-6903.
42. Porter, N.A. (1986). Mechanisms for the autoxidation of polyunsaturated lipids. *Acc. Chem. Res.* **19**, 262-268.
43. Jovanovic, S.V., Jankovic, I. & Josimovic, L. (1992). Electron-transfer reactions of alkyl peroxy radicals. *J. Am. Chem. Soc.* **114**, 9018-9021.
44. Garssen, G.J., Vliegenthart, J.F.G. & Boldingh, J. (1972). The origin of dimeric fatty acids from the anaerobic reaction between soya-bean lipoxygenase, linoleic acid and its hydroperoxide. *Biochem. J.* **130**, 435-442.
45. Jonas, R.T. & Stack, T.D.P. (1997). C-H bond activation by a ferric methoxide complex: a model for the rate-determining step in the mechanism of lipoxygenase. *J. Am. Chem. Soc.* **119**, 8566-8567.
46. Scarrow, R.C., *et al.*, & Nelson, M.J. (1994). X-Ray spectroscopy of the iron site in soybean lipoxygenase-1: changes in coordination upon oxidation or addition of methanol. *Biochemistry* **33**, 15023-15035.
47. Nelson, M.J., Chase, D.B. & Seitz, S.P. (1995). Photolysis of 'purple' lipoxygenase: Implications for the structure of the chromophore. *Biochemistry* **34**, 6159-6162.
48. Zhang, Y., Gebhard, M.S. & Solomon, E.I. (1991). Spectroscopic studies of the non-heme ferric active site in soybean lipoxygenase: magnetic circular dichroism as a probe of electronic and geometric structure. Ligand field origin of zero-field splitting. *J. Am. Chem. Soc.* **113**, 5162-5175.
49. Zhang, Y., Gan, Q-F., Pavel, E.G., Sigal, E. & Solomon, E.I. (1995). EPR definition of the non-heme ferric active sites of mammalian 15-lipoxygenase: major spectral differences relative to human 5-lipoxygenase and plant lipoxygenases and their ligand field origin. *J. Am. Chem. Soc.* **117**, 7422-7427.
50. Zang, Y., Elgren, T.E., Dong, Y. & Que, L.,Jr. (1993). A high-potential ferrous complex and its conversion to an alkylperoxoiron(III) intermediate. A lipoxygenase model. *J. Am. Chem. Soc.* **115**, 811-813.
51. Zang, Y., *et al.*, & Que, L.,Jr. (1997). Models for nonheme iron intermediates: structural basis for tuning the spin states of Fe(TPA) complexes. *J. Am. Chem. Soc.* **119**, 4197-4205.
52. Moiseyev, N., Rucker, J. & Glickman, M.H. (1997). Reduction of ferric ion could drive hydrogen tunneling in lipoxygenase catalysis: implications for enzymatic and chemical mechanisms. *J. Am. Chem. Soc.* **119**, 3853- 3860.
53. Solomon, E.I., Pavel, E.G., Loeb, K.E. & Campochiaro, C. (1995). Magnetic circular dichroism spectroscopy as a probe of the geometric and electronic structure of non-heme ferrous enzymes. *Coord. Chem. Rev.* **144**, 369-460.
54. Feig, A.L. & Lippard, S.J. (1994). Reactions of iron(II) centers with dioxygen in biology and chemistry. *Chem. Rev.* **94**, 759-805.
55. Dunham, W.R., Carroll, R.T., Thompson, J.F., Sands, R.H. & Funk, M.O., Jr. (1990). The initial characterization of the iron environment in lipoxygenase by Mössbauer spectroscopy. *Eur. J. Biochem.* **190**, 611-617.

56. Pavel, E.G. (1997). *Magnetic Circular Dichroism Spectroscopic Studies Of Mononuclear Non-Heme Iron Sites: Methodology And Applications To Non-Heme Enzymes*, Ph. D. Thesis. Stanford University.
57. Pavlosky, M.A., *et al.*, & Solomon, E.I. (1995). Near-infrared circular dichroism, magnetic circular dichroism, and X-ray absorption spectral comparison of the non-heme ferrous active sites of plant and mammalian 15-lipoxygenases. *J. Am. Chem. Soc.* **117**, 4316-4327.
58. Van der Heijdt, L.M., *et al.*, & Vliegenthart, J.F.G. (1992). X-Ray absorption spectroscopy of soybean lipoxygenase-1. *Eur. J. Biochem.* **207**, 793-802.
59. Scott, R.A. (1985). Measurement of metal-ligand distances by EXAFS. *Methods Enzymol.* **117**, 414-459.
60. Palmer, G. (1985). The electron paramagnetic resonance of metalloproteins. *Biochem. Soc. Trans.* **13**, 548-560.
61. Gaffney, B.J. & Silverstone, H.J. (1993). Simulation of the EMR spectra of high-spin iron in proteins. In *EMR of Paramagnetic Molecules* (Berliner, L.J., and Reuben, J., eds), 1-57, Plenum, New York.
62. Gaffney, B.J., Mavrophilipos, D.V. & Doctor, K.S. (1993). Access of ligands to the ferric center in lipoxygenase-1. *Biophys. J.* **64**, 773-783.
63. Nelson, M.J. (1988). Evidence for water coordinated to the active site iron in soybean lipoxygenase-1. *J. Am. Chem. Soc.* **110**, 2985-2986.
64. Nelson, M.J. (1987). The nitric oxide complex of ferrous soybean lipoxygenase-1. *J. Biol. Chem.* **262**, 12137-12143.
65. Hagen, W.R. (1992). EPR spectroscopy of iron-sulfur proteins. *Adv. Inorg. Chem.* **38**, 165-222.
66. Gebhard, M.S., Deaton, J.C., Koch, S.A., Millar, M. & Solomon, E.I. (1990). Single-crystal spectral studies of $Fe(SR)_4^-$ [R=2,3,5,6-$(Me)_4C_6H$]: the electronic structure of the ferric tetrathiolate active site. *J. Am. Chem. Soc.* **112**, 2217-2231
67. Deaton, J.C., Gebhard, M.S. & Solomon, E.I. (1989). Transverse and longitudinal Zeeman effect on $[PPh_4][FeCl_4]$: assignment of the ligand field transitions and the origin of the $^6A_1$ ground-state zero-field splitting. *Inorg. Chem.* **28**, 877-889.
68. Slappendel, S., Veldink, G.A., Vliegenthart, J.F.G., Aasa, R. & Malmström, B.G. (1980). EPR spectroscopy of soybean lipoxygenase-1. *Biochem. Biophys. Acta* **642**, 30-39.
69. Gardner, K.A., Mayer, J.M. (1995). Understanding C–H bond oxidations: hydrogen and hydride transfer in the oxidation of toluene by permanganate. *Science* **269**, 1849-1851.
70. Petersson, L., Slappendel, S., Feiters, M.C. & Vliegenthart, J.F.G. (1987). Magnetic susceptibility studies on yellow and anaerobically substrate-treated yellow soybean lipoxygenase-1. *Biochim. Biophys. Acta* **913**, 228-237.
71. Nelson, M.J. (1988). Catecholate complexes of ferric soybean lipoxygenase 1. *Biochemistry* **27**, 4273-4278.
72. Schewe, T., Wiesner, R. & Rapoport, S.M. (1981). Lipoxygenase from rabbit reticulocytes. *Methods Enzymol.* **71**, 430-441.